Applied Clay Science 168 (2019) 155–163

Contents lists available at ScienceDirect

Applied Clay Science

journal homepage: www.elsevier.com/locate/clay

Research Paper

Novel hierarchically porous allophane/diatomite nanocomposite for benzene adsorption

Liangliang Deng[a,b], Peixin Du[a,b], Wenbin Yu[c], Peng Yuan[a,b,*], Faïza Annabi-Bergaya[d], Dong Liu[a,b], Junming Zhou[a,b]

[a] CAS Key Laboratory of Mineralogy and Metallogeny/Guangdong Provincial Key Laboratory of Mineral Physics and Materials, Guangzhou Institute of Geochemistry, Chinese Academy of Sciences, Guangzhou 510640, China
[b] University of Chinese Academy of Sciences, 19 Yuquan Road, Beijing 100049, China
[c] State Key Laboratory of Ore Deposit Geochemistry, Institute of Geochemistry, Chinese Academy of Sciences, Guiyang, Guizhou 550081, China
[d] CNRS, UMR7374, Interface Confinement Matériaux et Nanostructures, 45071 Orléans, France

ARTICLE INFO

Keywords:
Allophane/diatomite nanocomposite
Allophane
Diatomite
Hierarchically porous structure
Benzene adsorption

ABSTRACT

Allophane/diatomite (Allo/Dt) nanocomposite with a hierarchically porous structure was prepared via an in situ hydrothermal method. This hierarchically porous structure consists of i) micropores remaining from the initial stacked coating allophane particles; ii) mesopores formed by the transformation of the macropores of diatom frustules due to the filling of allophane particles in the inner walls, and iii) preserved macropores of diatom frustules. The coating amount of allophane particles in Allo/Dt nanocomposite was 59.1%, leading to a specific surface area of 155.9 m^2/g, which was substantially higher than that of diatomite (17.9 m^2/g). The benzene adsorption performance and related adsorption mechanisms of Allo/Dt nanocomposite were investigated. The larger benzene dynamic adsorption capacity of 121.6 mg/g, compared to that of the synthetic allophane (105.9 mg/g), resulted from the adequate adsorption space provided by the hierarchically porous structure. Moreover, Allo/Dt nanocomposite displayed a higher efficiency for benzene adsorption in mesopores of the coating allophane particles because of their improved dispersity. These results demonstrated that the fabrication process of Allo/Dt nanocomposite can overcome not only the aggregation of allophane but also diatomite's shortcoming of low specific surface area, making the nanocomposite to be a promising adsorbent for the treatment of volatile organic compounds.

1. Introduction

The emission of volatile organic compounds (VOC), the most common air pollutants produced by petrochemical, chemical, pharmaceutical, and printing industries, has become a serious environmental problem, because they are toxic, hazardous, and even carcinogenic. VOC are the main sources of the photochemical reaction, and they can trigger the formation of secondary organic aerosols, which are harmful to human health (Pöschl, 2005; Kroll and Seinfeld, 2008; Hallquist et al., 2009). Hence, technologies for VOC control have gained much attention. Many technologies have been proposed for VOC control, such as membrane separation (Belaissaoui et al., 2016), oxidation (Kamal et al., 2016), biological treatment (Doble, 2006), and adsorption (Amari et al., 2010; Yu et al., 2015a) which is the most applicable technology because adsorption are low cost operation, low energy use, and flexible systems (Yu et al., 2015b).

The application of adsorption technology is dependent on the adsorbents used. Among the most commonly used adsorbents, activated carbon is the most versatile, owing to its low cost and excellent adsorption capacity. However, its utility is restricted by drawbacks such as fire risk, pore clogging, and regeneration difficulties (Zhao et al., 1998). Compared with activated carbon, synthetic zeolites such as SBA-15 (Dragoi et al., 2009) and ZSM-5 (Song et al., 2004; Serrano et al., 2007) have the advantages of controllable pore sizes and good chemical stability for VOC adsorption. However, the synthesis process of zeolites is complex, and their cost is very high, which hinder their wide application. Therefore, increasing awareness is focused on the development of adsorbents with low cost, good adsorption performance, and desirable thermal stability. Raw clay minerals with special porous structure have been proposed as alternative adsorbents, due to their excellent heat

* Corresponding author at: CAS Key Laboratory of Mineralogy and Metallogeny, Guangzhou Institute of Geochemistry, Chinese Academy of Sciences, Wushan, Guangzhou 510640, China.
E-mail address: yuanpeng@gig.ac.cn (P. Yuan).

https://doi.org/10.1016/j.clay.2018.11.007
Received 17 September 2018; Received in revised form 9 November 2018; Accepted 10 November 2018
Available online 17 November 2018

resistance and low cost (Deng et al., 2017).

Allophane ($1\text{-}2SiO_2{\cdot}Al_2O_3{\cdot}5\text{-}6H_2O$), a natural clay mineral widespread throughout the world, is a hydrated aluminosilicate. It has a hollow spherical structure with an outer diameter of 3.5–5.0 nm and a perforated wall about 0.7–1.0 nm thick (Nishikiori et al., 2009; Matsuura et al., 2013), meaning that the sphere contains a 1.5–3.6 nm diameter interior void. The wall of the hollow sphere is proposed to be composed of a curved gibbsite-like sheet with monomeric SiO_4 tetrahedra attached to it (Parfitt and Hemni, 1980; Johan et al., 1997). The wall surface features hydroxyl groups or hydration water and 0.3–0.5 nm-sized defect pores (Nishikiori et al., 2011). Due to the amphoteric ion-exchange activity, originating from the special wall structure, and the high specific surface area (SSA), allophane shows a high ability to adsorb ionic and polar pollutants such as Cu^{2+} (Okada et al., 2005), phosphate (Johan et al., 1997; Jara et al., 2006), arsenate (Arai et al., 2005), and acetate (Hanudin et al., 1999). In the field of VOC adsorption, adsorbents with large SSA and abundant micropores, which are regarded as important adsorption sites (Yang et al., 2014), usually display good adsorption performance. Although, high SSA of allophane and its well-developed microporous structure, including the defect pores and interior void, should be great advantages for VOC adsorption, the study on VOC adsorption of allophane has not been reported to date. Also, the adsorption performance of allophane and the related mechanisms are still not clear up to now. It is noteworthy that natural allophane is generally associated with other clay minerals such as imogolite and halloysite, which makes it difficult to obtain samples with a high purity. And, synthetic allophane, which is pure and can be readily obtained in large quantity, is suitable for the investigation of the adsorption performance of allophane.

Diatomite, also known as diatomaceous earth or kieselgur, is a fossil assemblage of diatom frustules with highly developed mesoporosity and/or macroporosity (Liu et al., 2012). It can be obtained easily at very low cost and possesses excellent thermal and mechanical stability (Yuan et al., 2013), and thus it is widely used as an adsorbent to remove aqueous pollutants, such as heavy metal ions (Dong and Zhang, 2013), dyes (Lin et al., 2007), arsenate (Pantoja et al., 2014), and methyl tertiary butyl ether (Aivalioti et al., 2010). Regarding VOC adsorption, diatomite shows relatively low mass transfer resistance and a rapid diffusion rate, due to its macroporous structure (Yuan et al., 2016). However, the VOC adsorption capacity of diatomite is limited by its relatively low SSA (Yuan et al., 2015b). Previous studies have shown that diatomite is an excellent support, and it thus would seem possible to fabricate composites with high SSA and outstanding adsorption performance by using diatomite as a support to coat nanoparticles (Yuan et al., 2010; Hadjar et al., 2011).

In this study, an allophane/diatomite (Allo/Dt) nanocomposite was obtained, creating a hierarchically porous structure combining the advantages of the high SSA and well-developed microporous structure of synthetic allophane (Allo) and the excellent supporting property of diatomite (Dt). X-ray diffraction (XRD), scanning electron microscopy (SEM), transmission electron microscopy (TEM), selected-area electron diffraction (SAED), N_2 adsorption-desorption, Fourier-transform infrared (FTIR) spectroscopy and diffuse reflectance infrared Fourier-transform (DRIFT) spectroscopy were adopted to characterize the structural features and surface properties of Allo/Dt nanocomposite. Benzene, a commonly used solvent in industrial processes which ranks at the top of the list of VOC pollutants, was selected as a model organic pollutant to investigate the dynamic adsorption performance of Allo/Dt nanocomposite and the related adsorption mechanisms via breakthrough curve method.

2. Experiment

2.1. Materials

Poly(diallyldimethylammoniumchloride) (PDDA, 20mass% in water) was purchased from Aldrich. Sodium orthosilicate (Na_4SiO_4) was provided by Alfa Aesar. Aluminum chloride hexahydrate ($AlCl_3{\cdot}6H_2O$, 99%) was supplied by Guangzhou Chemical Reagent Co., Ltd. Raw diatomite was obtained from Qingshanyuan Diatomite Co., Ltd. (Jilin province, China) and purified using the sedimentation method (Yuan et al., 2006).

2.2. Preparation of Allo and Allo/Dt nanocomposite

Allo was synthesized following the previously reported procedure (Ohashi et al., 2002). Aluminum chloride hexahydrate and sodium orthosilicate were prepared at an initial concentration of 100 mmol/L as Al-source and Si-source solutions, respectively. Next, the Al-source and Si-source solutions were mixed together rapidly at an Al/Si molar ratio of 4/3 with stirring for 1 h. Subsequent centrifugation was conducted at a speed of 4000 rpm for 10 min to remove the byproduct NaCl, yielding allophane precursor gel. The gel was then autoclaved at 100 °C for 48 h. Subsequently, the autoclaved gel was repeatedly washed with distilled water until it reached a neutral pH, and then freeze-drying and grinding were performed to obtain the allophane powder.

The synthesis steps of Allo/Dt nanocomposite were as follows: first, 2.0 g of Dt was added into 80 mL of 0.5mass% PDDA solution, and the dispersion was stirred vigorously for approximately 1 h to allow surface modification. It was then dried and mixed with 400 mL of the Al-source solution. To guarantee the Al/Si molar ratio was 4/3, 300 mL of the Si-source solution was added into the dispersion at a rate of 10 mL/min, accompanied by stirring at a speed of 500 rpm. The mixture was further stirred for 1 h at room temperature after the Si-source solution was completely added. Finally, Allo/Dt nanocomposite was synthesized after centrifugation, hydrothermal reaction, washing, freeze-drying and grinding were performed in the same manner as in the preparation of Allo.

2.3. Characterization methods

Major element oxides were analyzed using a Rigaku RIX 2000 X-ray fluorescence spectrometer (XRF) on fused glass beads. Calibration lines used in quantification were produced by bivariate regression of data from 36 reference materials encompassing a wide range of silicate compositions. Analytical uncertainties were mostly between 1% and 5%.

The XRD patterns were recorded on a Bruker D8 Advance diffractometer with a Ni filter and Cu-Kα radiation ($\lambda = 0.154$ nm) using a generator voltage of 40 kV and a current of 40 mA. The scan rate was 3° (2θ)/min.

N_2 adsorption-desorption isotherms were measured with a Micromeritics ASAP2020 system at liquid-nitrogen temperature. To completely remove the physically adsorbed water, the samples were outgassed at 120 °C for 12 h before measurements (Du et al., 2018). The SSA (S_{BET}) of the samples were calculated from the nitrogen adsorption data using the multiple-point Brunauer-Emmett-Teller (BET) method (Brunauer et al., 1938), and the total pore volume (V_{total}) was estimated based on the nitrogen uptake at a relative pressure of approximately 0.97. The microporous surface area (S_{micro}) and micropore volume (V_{micro}) of the samples were derived from *t*-plot method. Barrett-Joyner-Halenda (BJH) method (Gregg and Sing, 1982) was used to calculate the mesoporous surface area (S_{meso}) and mesopore volume (V_{meso}). The non-local density functional theory (NLDFT) model (Thommes et al., 2015) was used to determine the micropore and mesopore size distributions of Allo and Allo/Dt nanocomposite.

Scanning electron microscope (SEM) micrographs were obtained using a SU8010 cold field emission scanning electron microscope (FESEM, Hitachi, Japan). The specimens for SEM observation were anchored on the surface of the conducting tape, and then transferred directly into the microscope.

Transmission electron microscopy (TEM) and selected-area electron

diffraction (SAED) analyses were carried out using a FEI Talos F200S field-emission transmission electron microscope operating at an accelerating voltage of 200 kV. The specimens for TEM observation were prepared using the following procedure. The sample was ultrasonically dispersed in ethanol for 5 min, then a drop of sample dispersion was dropped onto a carbon-coated copper grid, which was left to stand for 10 min and transferred into the microscope.

Fourier-transform infrared (FTIR) spectra were recorded on a Bruker Vertex 70 IR spectrometer. The specimens used for FTIR measurement were prepared by mixing 0.9 mg of sample powder with 80.0 mg of KBr and pressing the mixture into a pellet. For each FTIR measurement, 64 scans were collected over the range of 400–4000 cm^{-1} at a resolution of 4 cm^{-1}. Diffuse reflectance infrared Fourier-transform (DRIFT) spectra were obtained on the diffuse reflectance attachment. A portion of the powder was packed lightly into a 4 mm inner-diameter micro sample cup for DRIFT spectra collection, and the spectra were collected over the range of 600–4000 cm^{-1} with 64 scans and a resolution of 4 cm^{-1} and normalized against a KBr background reference.

2.4. Benzene adsorption test

The benzene adsorption performance of the samples was evaluated using an in-line gas chromatography apparatus (Fig. 1) (Hu et al., 2009). Before the adsorption process, the samples were heated at 120 °C in a muffle oven for 2 h, which was able to remove most of the physically adsorbed water molecules and small organic impurities adsorbed in pores. During the adsorption measurement, the organic saturator with benzene was immersed in a water bath at 30 °C. Each powder sample weighed approximately 0.5 g and was loaded in a glass column. The column was fed with a dry nitrogen stream containing benzene vapor at 3.00 mL/min, which could be adjusted by Mass Flow Controller (MFC). The concentrations of benzene in both the column influent and effluent were quantified using a gas chromatograph (Agilent 7820A) with a flame ionization detector (FID). The experiment was stopped when the adsorption equilibrium was reached. After the adsorption, the glass column containing the sample was heated at 120 °C for 12 h to ensure the complete desorption of adsorbed benzene molecules and then retested. This process was repeated for 4 times to evaluate the regeneration performance of Allo/Dt nanocomposite.

The benzene adsorption capacity (q, mg/g) of the adsorbents was calculated by integrating the area above the acquired breakthrough curve after subtracting the area attributed to the system dead volume, according to the following equation.

$$q = \frac{M}{1000m}\int_{t_1}^{t_2} F[C_0 - C_t]dt \quad (1)$$

where M (g/mol) is the molecular mass of benzene, m (g) is the initial mass of the adsorbents before the test, t_1 (min) is the breakthrough time without the samples, t_2 (min) is the breakthrough time with the packed column, C_0 and C_t (mmol/L) represent the influent and measured effluent benzene concentrations, respectively, and F (mL/min) is the N_2 flow rate. The dead space was obtained by performing blank runs without the column.

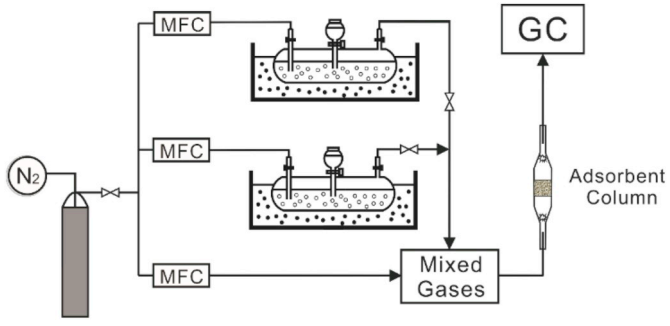

Fig. 1. Schematic diagram of experimental set-up. MFC: mass flow controller.

The breakthrough curves were fitted using Yoon and Nelson model (Yoon and Nelson, 1984).

$$t = \tau + \frac{1}{k}\ln\frac{C_t}{C_0 - C_t} \quad (2)$$

where t (min) is the breakthrough time, C_t and C_0 are the outlet and inlet concentrations of the stream through the adsorbent column, τ (min) is the time when the breakthrough concentration reached half of the initial concentration ($C_t = 0.5C_0$), and k is a mass transfer coefficient.

3. Results and discussion

3.1. Compositional and morphological characteristics of Allo/Dt nanocomposite

The XRD pattern of Dt (Fig. 2a) revealed the main phase of non-crystalline opal-A with a characteristic broad reflection centered at 4.1 Å. Quartz impurity with a content of approx. 4%, which was semi-quantitatively determined, was also present. The XRD pattern of Allo (Fig. 2a) showed a broad reflection at 3.3 Å and a weak one at 2.3 Å. The former reflection corresponded to an interference between neighboring SiO tetrahedra (Henmi et al., 1981). The latter weak reflection might arise from a structure similar to the imogolite local structure (Du et al., 2017). These results were consistent with the diffraction pattern of allophane synthesized by Ohashi et al. (2002). In the XRD pattern of Allo/Dt nanocomposite (Fig. 2a), a broadened reflection at 3.7 Å could be observed as well as a weak characteristic reflection of allophane at 2.3 Å. The broadening of the reflection at 3.7 Å could be attributed to the overlapping of the corresponding characteristic reflections of diatomite and allophane. These results indicated the existence of remaining diatomite and allophane in the Allo/Dt nanocomposite.

The FTIR spectra of Dt, Allo, and Allo/Dt nanocomposite are displayed in Fig. 2b, and the assignments of each vibration are based on previous reports on diatomite and allophane (Farmer et al., 1979; Parfitt, 1990; Iyoda et al., 2012; Bishop et al., 2013; Yuan et al., 2013). The spectrum of Dt (Fig. 2b) presented a broad band centered at 3436 cm^{-1} in the hydroxyl region (3000–4000 cm^{-1}) and a weak one at 1635 cm^{-1}, which could be ascribed to the O—H stretching and O—H deformation of physically absorbed water, respectively. The band at 1100 cm^{-1} corresponded to the in-plane Si—O stretching, and the band at 800 cm^{-1} reflected the symmetric Si—O stretching. The vibration at 470 cm^{-1} was caused by Si–O–Si deformation. In the spectrum of Allo (Fig. 2b), the broad band at 3468 cm^{-1} was due to the O—H stretching vibrations of Si—OH, Al—OH, and associated adsorbed water. The appearance of the O—H deformation vibration at 1635 cm^{-1} confirmed the existence of adsorbed water in Allo. In addition to the bands at 3468 and 1635 cm^{-1}, three bands at 966, 565, and 430 cm^{-1} could be observed in the spectrum of Allo (Fig. 2b). They were all characteristic bands of allophane (Thill, 2016; Du et al., 2018) and could be ascribed to Si—O stretching vibration, Al-O-Si deformation (Rampe et al., 2012), and O-Si-O bending vibration, respectively. The spectrum of Allo/Dt nanocomposite (Fig. 2b) showed the characteristic bands of both Dt (1100, 800 and 470 cm^{-1}) and Allo (a shoulder at 966 cm^{-1} and a weak band at 565 cm^{-1}), confirming the presence of diatomite and allophane. Moreover, the emergence of the bands at 3449 and 1635 cm^{-1} demonstrated the existence of a certain amount of hydroxyl groups and/or adsorbed water in Allo/Dt nanocomposite, indicating that Allo/Dt nanocomposite was hydrophilic.

As shown in Table 1, the Al_2O_3 content of Dt was 2.49%, and its Al/Si molar ratio was only 0.03. These results indicated that there was a small amount of Al in Dt, which could be ascribed to the structural Al in diatomite. Allo had the highest Al_2O_3 content (37.76%, Table 1), and its Al/Si molar ratio was 1.3, implying that Allo was a mixture of unit

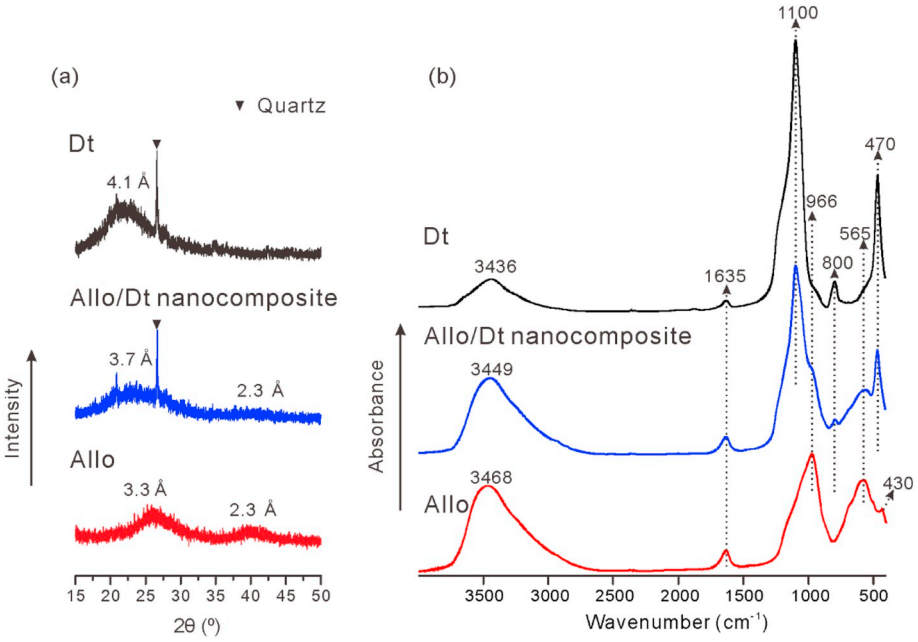

Fig. 2. (a) XRD patterns and (b) FTIR absorbance spectra of Dt, Allo, and Allo/Dt nanocomposite.

particles or of structures within particles of Al-rich allophane and Si-rich allophane (Parfitt, 1990; Du et al., 2018). The Al_2O_3 content and Al/Si molar ratio of Allo/Dt nanocomposite (22.48% and 0.41, respectively) increased significantly compared with those of Dt (2.49% and 0.03, respectively), due to the existence of allophane. In addition, the coating amount of allophane in Allo/Dt nanocomposite was 59.1%, which was calculated based on Al_2O_3 and SiO_2 content and the Al/Si molar ratio of Dt, Allo, and Allo/Dt nanocomposite.

As shown in the SEM image in Fig. 3a, the dominant diatom in Dt, classified as *Coscinodiscus Ehrenberg* (*Centrales*), was disc-shaped, and it had highly developed macropores with regular pore diameters (0.1–0.8 μm). The diatom frustules were relatively uniform in particle diameter (20–40 μm) and thickness (1.2–1.8 μm), as determined in previous work (Yuan et al., 2013). The SEM image of Allo (Fig. 3b) displayed a great number of spherical particles with diameters of tens of nanometers, and these particles aggregated severely, forming numerous pores with irregular and non-uniform channels. The TEM image of Allo given in Fig. 3c revealed a hollow structure in the spherical particles, and a broad and isotropic halo in the SAED pattern of the spherical particles (inset in Fig. 3c), indicating that these spherical particles were amorphous. These results were in accordance with the allophane synthesized by Iyoda et al. (2012). Fig. 3d provided the SEM images of Allo/Dt nanocomposite and showed that the surface of the diatom frustule were completely coated with spherical particles. These spherical particles correspond to the allophane particles, according to the analysis results of XRD and FTIR (Fig. 2a and b). As observed at a higher magnification (Fig. 3d), the allophane particles coated on the surface of diatom frustule in Allo/Dt nanocomposite dispersed much better (Fig. 3b), indicating the improvement of dispersity of allophane particles due to the support of diatomite. Additionally, some macropores of the diatom frustules were preserved in Allo/Dt nanocomposite, and some mesopores were introduced by the transformation from the macropores of diatom frustules, due to the filling of allophane particles in the inner wall. These results demonstrated that Allo/Dt nanocomposite had a hierarchically porous structure. The TEM images of Allo/Dt nanocomposite (Fig. 3e) clearly displayed the filled allophane particles and confirmed the existence of the hierarchically porous structure.

3.2. Hierarchically porous structure of Allo/Dt nanocomposite

The N_2 adsorption-desorption isotherms of Dt, Allo, and Allo/Dt nanocomposite are shown in Fig. 4a. The isotherm of Dt was characterized as type II with H3 hysteresis loop, according to the IUPAC classification refined by Thommes et al. (2015). The hysteresis loop was associated with the filling and emptying of mesopores by capillary condensation, indicating the existence of mesopores arising from the diatom frustules. The sharp increase in the amount of adsorbed N_2 near the relative pressure of one ($P/P_0 = 1$) corresponded to adsorption by the macropores of diatom frustules. The isotherm of Allo could be classified as type I(b) with the smallest H4 hysteresis loop, corresponding to limited mesopores. The mesopores of Allo might be formed by the disordered stacking of allophane particles. The rapidly increased adsorption quantities at relatively low pressure ($P/P_0 < 0.1$) suggested the presence of massive micropores. As previous studies of the morphology and structure of allophane had shown, there were 0.3–0.5 nm-sized defect pores on the wall surface and an interior void with a diameter of 1.5–3.6 nm in the sphere (Ohashi et al., 2002; Montarges-

Table 1
Chemical compositions of Dt, Allo, and Allo/Dt nanocomposite.

Sample	Chemical compositions (mass %)								
	SiO_2	Al_2O_3	Fe_2O_3	MgO	CaO	Na_2O	K_2O	TiO_2	L.O.I.*
Dt	89.52	2.49	0.24	0.12	0.18	0.48	0.68	0.15	5.91
Allo	34.32	37.76	0.01	0.01	0.05	0.27	0.01	0.01	27.40
Allo/Dt nanocomposite	54.80	22.48	0.10	0.07	0.17	0.46	0.46	0.04	21.20

L.O.I.* denotes loss on ignition.

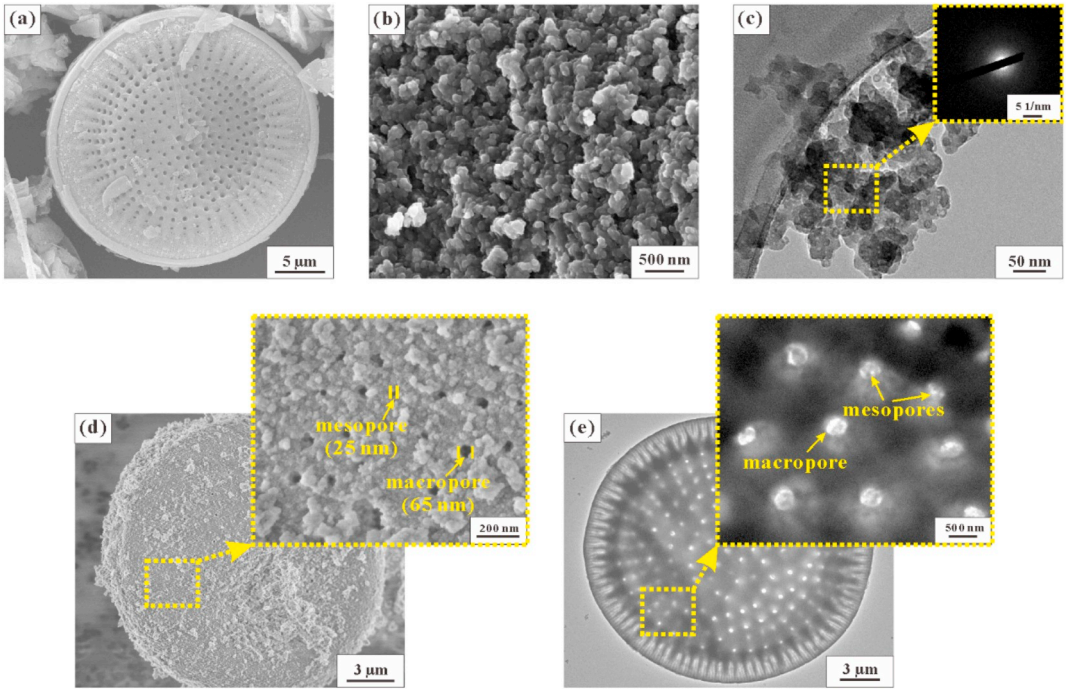

Fig. 3. SEM images of (a) Dt, (b) Allo, and (d) Allo/Dt nanocomposite; and TEM images of (c) Allo and (e) Allo/Dt nanocomposite.

Pelletier et al., 2005; Kawachi et al., 2013). Therefore, if the nitrogen molecules could penetrate the defect pores into the interior void, the hysteresis loop of the isotherm of Allo should belong to type H2, which is related to the ink-bottle pore structure (Thommes et al., 2015). However, the hysteresis loop of the isotherm of Allo was type H4, which is associated with aggregated particles. These results indicated that the nitrogen molecules cannot get through the defect pores due to hampering from the hydroxyl groups and/or adsorbed water on the surface, as the FTIR spectrum of Allo indicated (Fig. 2b), and the micropores of Allo could mainly be attributed to the stacking of allophane particles. Moreover, the amount of the adsorbed N_2 near $P/P_0 = 1$, also increased sharply, implying the existence of macropores in Allo. These macropores could be ascribed to the stacking of aggregates of allophane particles. After the compounding of diatomite and allophane, the isotherm of Allo/Dt nanocomposite changed to type IV(a) with a H4 hysteresis loop. Moreover, the hysteresis loop of Allo/Dt nanocomposite formed at a lower pressure ($P/P_0 \approx 0.4$) compared with those of Dt and Allo, suggesting that Allo/Dt nanocomposite had a more extensive mesopore size distribution than Dt and Allo. The mesopores of Allo/Dt nanocomposite might result from the stacking of the coating allophane particles and the transformation of the macropores of diatom frustules, owing to the filling of allophane particles in the inner wall, as the SEM (Fig. 3d) and TEM (Fig. 3e) images revealed. The N_2 adsorption quantity of Allo/Dt nanocomposite at relatively low pressures ($P/P_0 < 0.1$) was less than that of Allo, implying fewer micropores in Allo/Dt nanocomposite than in Allo. The rapid increase of the amount of adsorbed N_2 near $P/P_0 = 1$, could be attributed to the preserved macropores of diatom frustules in Allo/Dt nanocomposite.

Fig. 4b displays the NLDFT pore size distribution (PSD) curves of Allo and Allo/Dt nanocomposite in the range from 0.35 to 50.00 nm. However, the PSD curve of Dt was not shown in Fig. 4b, because diatomite is mainly characterized by macroporosity, and the pore distribution centers of Dt were very inconspicuous. As exhibited in Fig. 4b, the PSD curve of Allo revealed some micropore distribution centers (0.63, 0.88, 1.03, 1.56, and 1.75 nm, respectively) and a mesopore distribution center (27.30 nm), indicating the existence of a great number of micropores and a small amount of mesopores in Allo. This result was in accordance with the N_2 adsorption-desorption isotherms of Allo (Fig. 4a), which showed steeply increased adsorption quantities at relatively low pressures ($P/P_0 < 0.1$) and the smallest hysteresis loop. The micropores and mesopores of Allo could all be attributed to the stacking of allophane particles. Compared with the PSD curve of

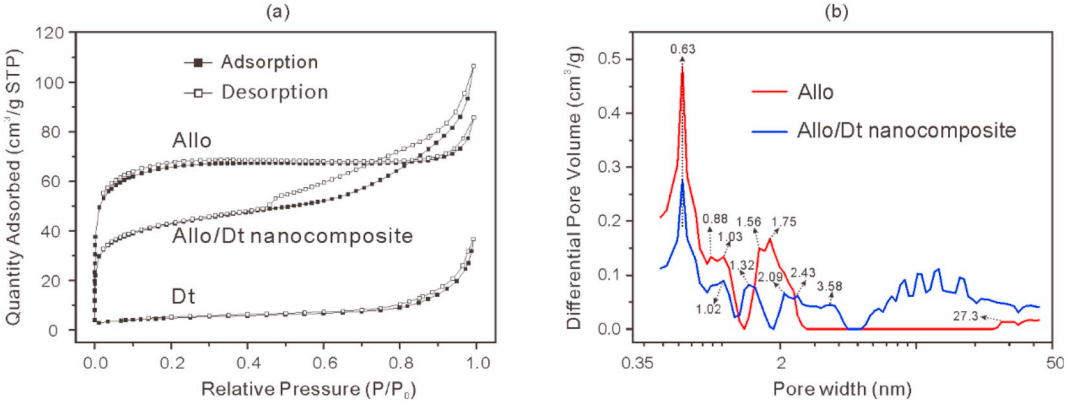

Fig. 4. (a) N_2 adsorption-desorption isotherms and (b) NLDFT pore size distribution (PSD) curves of Dt, Allo, and Allo/Dt nanocomposite.

Table 2
Porous parameters of Dt, Allo, and Allo/Dt nanocomposite.

Samples	S_{BET} (m^2/g)	V_{total} (cm^3/g)	S_{micro}[a] (m^2/g)	V_{micro}[a] (cm^3/g)	S_{meso}[b] (m^2/g)	V_{meso}[b] (cm^3/g)
Dt	17.9	0.031	5.5	0.002	9.5	0.029
Allo	242.6	0.120	183.8	0.075	2.0	0.009
Allo/Dt nanocomposite	155.9	0.144	95.3	0.039	29.5	0.055

[a] The microporous specific surface area and micropore volume were calculated using the *t*-plot method.
[b] The mesoporous specific surface area and mesopore volume were calculated using the BJH method.

Allo, the amount of micropore distribution centers on the PSD curve of Allo/Dt nanocomposite decreased, but many more new mesopore distribution centers appeared, especially some relatively small mesopores with pore sizes of < 5 nm (2.03, 2.43, and 3.58 nm, respectively). These results indicated that Allo/Dt nanocomposite not only retained the micropores of allophane particles but also had an extensive mesoporous structure, which was consistent with the results of N_2 adsorption-desorption isotherms (Fig. 4a). The reduction of micropores could be attributed to the decrease of the relative content of allophane. However, the emergence of newly formed mesopores might be explained by the improved dispersity of the coating allophane particles, which contributed to the formation of mesopores with smaller pore sizes, and the transformation of macropores resulting from the filling of the allophane particles in the inner wall of diatom frustules, which could be observed in the SEM (Fig. 3d) and TEM (Fig. 3e) images.

As shown in Table 2, the S_{BET} of Dt of 17.9 m^2/g was the lowest among the three samples, because diatomite is characterized by a macro/mesoporous structure (Yuan et al., 2010). In contrast, Allo had the highest S_{BET} (242.6 m^2/g) and S_{micro} (183.8 m^2/g) as shown in Table 2. These results indicated that the S_{BET} of Allo was mainly due to the micropores. However, the S_{BET} of Allo was lower than the theoretical value (~1000 m^2/g) calculated from geometry of allophane, owing to the small size of defect pores and the special surface of allophane (Du et al., 2018). The diameter of N_2 molecule (0.36 nm) is larger than the smallest diameter of the defect pores (0.35 nm) that there might be steric effects for N_2 molecule to detect the surface of the interior void of allophane. In addition, as shown in the FTIR spectrum of Allo (Fig. 2b), a certain amount of hydroxyl groups and/or adsorbed water existed on the surface, which prevented N_2 molecules from penetrating into the void through the defect pores, making the N_2 adsorption technique fail in well detecting the surface of interior void.

Despite having the highest S_{BET} and S_{micro}, Allo showed the lowest S_{meso} (2.0 m^2/g) and V_{meso} (0.009 cm^3/g) (Table 2), suggesting that Allo had the least developed mesoporous structure among these three samples. This result was consistent with the N_2 adsorption-desorption isotherms of Allo displaying the smallest hysteresis loop (Fig. 4a). As the allophane particles were introduced into the Dt, the S_{BET} and S_{micro} of Allo/Dt nanocomposite (155.9 and 95.3 m^2/g, respectively) were distinctly higher than those of Dt (17.9 and 5.5 m^2/g, respectively), but were still lower than those of Allo (242.6 and 183.8 m^2/g, respectively), indicating the less developed microporosity of Allo/Dt nanocomposite compared with Allo. However, the S_{meso} of Allo/Dt nanocomposite (29.5 cm^2/g) was noticeably higher than those of Dt and Allo (9.5 and 2.0 m^2/g, respectively) because of enhanced mesoporosity, owing to the improved dispersity of the coating allophane particles and the transformation of some macropores of diatom frustules into mesopores.

3.3. Benzene adsorption performance of Allo/Dt nanocomposite and related mechanisms

The breakthrough curves of Dt, Allo, and Allo/Dt nanocomposite (Fig. 5) were used to evaluate their dynamic benzene adsorption capacity (*q* value, Table 3). As Table 3 indicates, the *q* value of Dt was the lowest (74.5 mg/g), because the adsorption reaction of Dt was mainly caused by surface adsorption, and Dt had the smallest S_{BET},

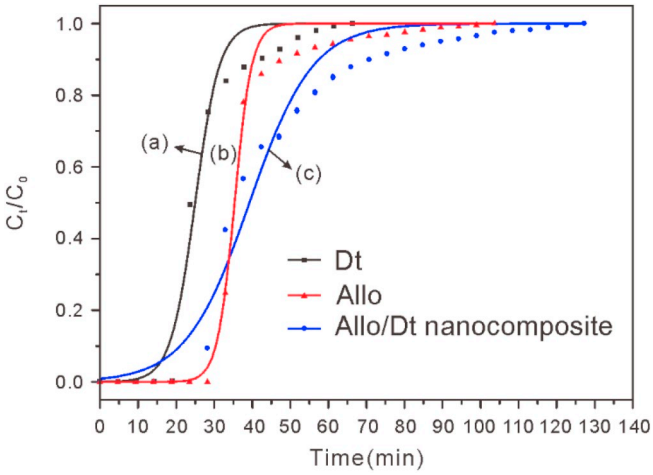

Fig. 5. Breakthrough curves of (a) Dt; (b) Allo; (c) Allo/Dt nanocomposite.

Table 3
Dynamic adsorption capacity (*q*) and Yoon and Nelson equation parameters for benzene adsorption of Dt, Allo, and Allo/Dt nanocomposite.

Sample	*q* (mg/g)	q_s(mg/g)	*k*	τ (min)	R^2
Dt	74.5	–	0.317	25.11	0.979
Allo	105.9	105.9	0.445	35.35	0.990
Allo/Dt nanocomposite	121.6	205.8	0.120	39.28	0.973

corresponding to the smallest number of adsorption sites. The *q* value of Allo (105.9 mg/g) was higher than that of Dt (74.5 mg/g, Table 3), owing to its largest S_{BET} and massive micropores. Allo/Dt nanocomposite showed the largest *q* value (121.6 mg/g), even though its S_{BET} and S_{micro} (155.9 and 95.3 m^2/g, respectively, Table 2) were lower than those of Allo (242.6 and 183.8 m^2/g, respectively, Table 2). These results implied that not all the micropores of Allo acted as adsorption sites for benzene molecules, although the pore sizes of most micropores (0.63, 0.88, 1.03, 1.56 and 1.75 nm) were larger than the kinetic diameter of benzene molecule (0.59 nm). The reason might be that the micropores of Allo derived from the disordered stacking of allophane particles, and their channels were very inhomogeneous, as the SEM image (Fig. 3b) showed. It was much easier for the micropores to adsorb nitrogen molecules, which have a smaller size of 0.36 nm than benzene molecules. In addition, the surface of allophane particles was hydrophilic, owing to the existence of hydroxyl groups and/or adsorbed water, and it exhibited poor adsorption affinity for the hydrophobic benzene molecules (Yu et al., 2015c). Concerning Allo/Dt nanocomposite, its hierarchically porous structure could provide adequate space for benzene adsorption, especially the abundant mesopores, which could adsorb benzene molecules by capillary condensation. Moreover, in the consideration of the allophane coating amount of Allo/Dt nanocomposite of 59.1%, the normalized dynamic benzene adsorption capacity of Allo/Dt nanocomposite (q_s value, Table 3) increased to 205.8 mg/g, which was almost twice that of Allo (105.9 mg/g, Table 3). This result indicated the higher allophane utilization

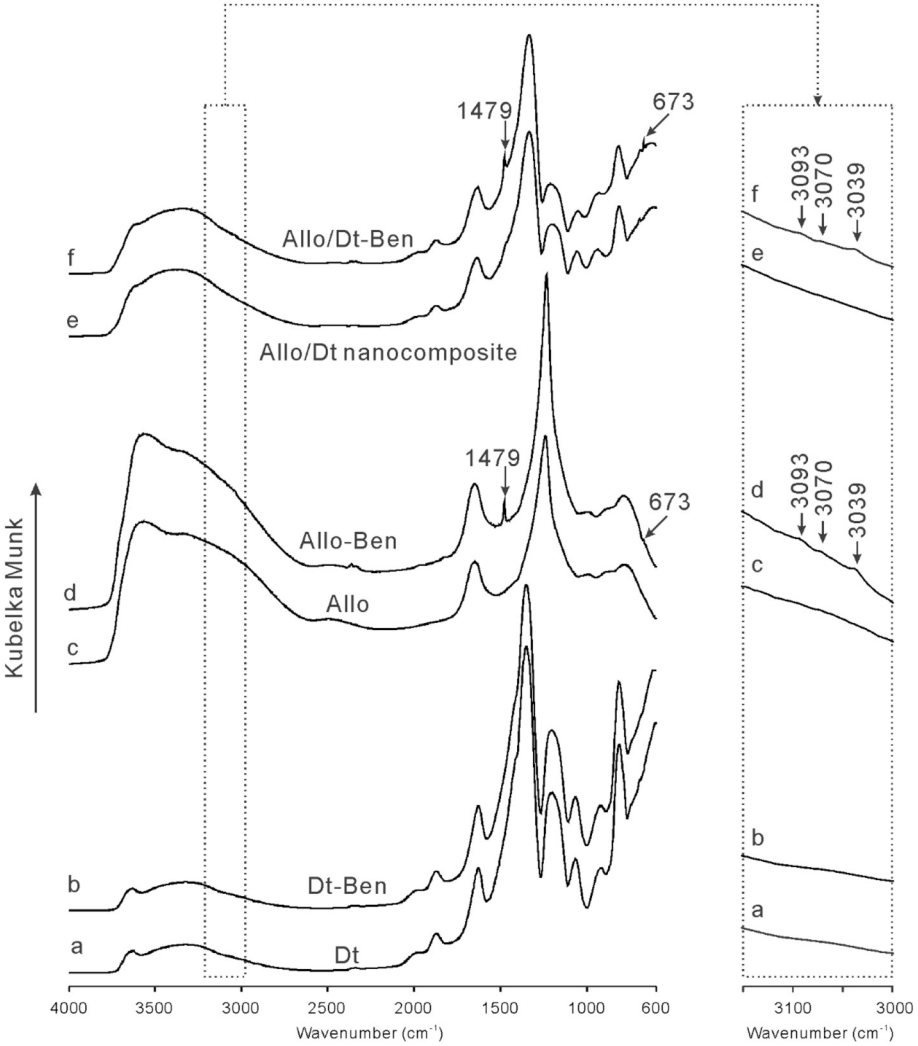

Fig. 6. DRIFT spectra of (a) Dt; (b) Dt-Ben; (c) Allo; (d) Allo-Ben; (e) Allo/Dt nanocomposite; (f) Allo/Dt-Ben.

efficiency of Allo/Dt nanocomposite. In this nanocomposite, the allophane particles were distributed uniformly on the surface of the diatomite supports, resulting in improved dispersity of the coating allophane particles. Therefore, the coating allophane particles could more fully come into contact with the benzene molecules, which enables higher allophane utilization efficiency for Allo/Dt nanocomposite than for Allo.

To detect interactions between benzene molecules and these three absorbents, DRIFT characterization was performed. The obtained samples after Dt, Allo, and Allo/Dt nanocomposite adsorbed benzene were named Dt-Ben, Allo-Ben, and Allo/Dt-Ben, respectively. As shown in Fig. 6a and b, no significant change occurred between the DRIFT spectra of Dt and Dt-Ben, indicating that no benzene molecules were detected on the surface of Dt-Ben. This result might be due to the lowest benzene adsorption capacity of Dt. However, the characteristic vibrational bands of benzene, including C—H stretching (3093, 3070 and 3039 cm^{-1}) and C=C stretching (1479 and 673 cm^{-1}) of the aromatic rings (Palazov, 1973; De Mallmann and Barthomeuf, 1988; Du et al., 2002), appeared on the DRIFT spectra of Allo-Ben (Fig. 6d) and Allo/Dt-Ben (Fig. 6f). This result confirmed that benzene adsorption occurred in Allo and Allo/Dt nanocomposite. Apart from the emergence of the characteristic vibrational bands of benzene, other bands on the spectra of Allo-Ben and Allo/Dt-Ben are the same as those on the spectra of Allo (Fig. 6c) and Allo/Dt nanocomposite (Fig. 6e), indicating that chemical bonds were not formed and the adsorption type of benzene on Allo and Allo/Dt nanocomposite belongs to physical adsorption.

The evaluation for the regeneration performance of VOC adsorbents is an importance factor for their industrial application. The breakthrough process of benzene adsorption over Allo/Dt nanocomposite was performed for 4 times (Fig. 7). As Fig. 7 displayed, the breakthrough curves of Allo/Dt nanocomposite exhibited a relatively good repeatability over 4 cycles of benzene adsorption. In addition, the recycling efficiency of Allo/Dt nanocomposite after 4 cycles of benzene adsorption could still reached 89.5% (Table 4). These results indicated the good regeneration performance of Allo/Dt nanocomposite, which might be attributed to its hierarchically porous structure and adsorption type (physical adsorption). The hierarchically porous structure, especially the macropores, is conducive to the desorption of benzene molecules, and the force of physical adsorption is generally weaker than that of chemical adsorption, which is favourable to the regeneration of VOC adsorbents. Therefore, compared to activated carbon that mainly possessed micropores and could interact with VOC molecules by similar chemical behaviour through the surface functional groups (GarcíA et al., 2004; Lillo-Ródenas et al., 2005), Allo/Dt nanocomposite might have great advantages in regeneration.

The porous structure of VOC adsorbents plays an important role in their adsorption performance. Previous studies have investigated the dynamic adsorption of benzene by various clay minerals, such as kaolinite (Kaol), halloysite (Hal), and montmorillonite (Mt); and the

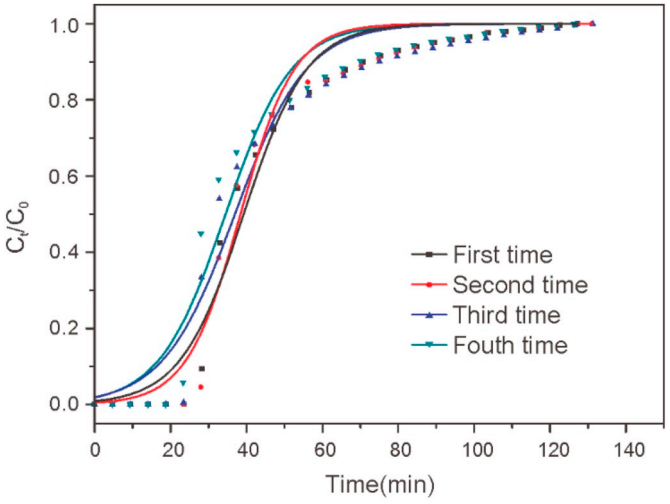

Fig. 7. Benzene adsorption breakthrough curves of Allo/Dt nanocomposite cycled for 4 times.

Table 4
Dynamic adsorption capacity (q) and Yoon and Nelson equation parameters for various cycles of Allo/Dt nanocomposite.

Cycles	q (mg/g)	k	τ (min)	R^2	Efficiency (%)
First	121.6	0.120	39.28	0.973	–
Second	120.7	0.141	38.43	0.972	99.3%
Third	117.3	0.106	36.96	0.959	96.5%
Fourth	108.8	0.115	34.48	0.959	89.5%

reported dynamic adsorption capacity of Kaol, Hal, and Mt. were 56.7, 68.1 and 141.2 mg/g, respectively (Deng et al., 2017). This study has found that the dynamic adsorption capacity of Allo/Dt nanocomposite (121.6 mg/g, Table 3) was higher than that of Kaol (56.7 mg/g) and Hal (68.1 mg/g), but lower than that of Mt (141.2 mg/g). These results were due to the different porous structures of these samples. According to the study of Deng et al. (2017), the microporosity of Kaol was so small that its benzene adsorption mainly occurred at the external surface, and its S_{BET} was very small (17.9 m^2/g). Therefore, the dynamic adsorption capacity of Kaol (56.7 mg/g) was lower than that of Allo/Dt nanocomposite. Hal had a mesoscopic lumen with a diameter of ~20 nm and some slit-shaped micropores resulting from dehydration (Yuan et al., 2012, 2015a; Deng et al., 2017), but because the size of the lumen was considerably bigger than the diameter of benzene molecule (0.59 nm), the effect of capillary condensation of Hal was weaker than that of Allo/Dt nanocomposite with various small mesopores (2.09, 2.43 and 3.58 nm, Fig. 4b). Furthermore, the slit-shaped micropores of Hal could not accommodate benzene molecules. Thus, the dynamic adsorption performance of Hal was also poorer than that of Allo/Dt nanocomposite. Mt. showed a higher dynamic adsorption capacity (141.2 mg/g) than Allo/Dt nanocomposite, because its interlayer micropores were available for benzene adsorption, while only some of the micropores of Allo/Dt nanocomposite could host benzene adsorption. However, it is worth noting that Mt. would exhibit a sieving effect for VOC adsorption (Deng et al., 2017). In other words, Mt. could only adsorb VOC molecules with a diameter smaller than the size of the interlayer micropores. Therefore, Allo/Dt nanocomposite might have better adsorption performance than Mt. in the adsorption of VOC molecules with the size larger than that of the interlayer micropores of Mt., due to the existence of hierarchically porous structure. An investigation of the effect of VOC molecule size on the VOC adsorption performance of Allo/Dt nanocomposite is currently underway.

4. Conclusion

In this study, allophane/diatomite nanocomposite with a hierarchically porous structure was prepared, and its dynamic adsorption of benzene and the related adsorption mechanism were investigated. Allophane particles were well distributed on the surface of diatom frustules and filled in the inner wall of macropores, resulting in the formation of a hierarchically porous allophane/diatomite nanocomposite with relatively high S_{BET}. The prepared allophane/diatomite nanocomposite exhibited higher dynamic benzene adsorption capacity and allophane utilization efficiency than synthetic allophane. The hierarchically porous structure of allophane/diatomite nanocomposite makes it have the potential to adsorb VOC of various sizes and become an efficient VOC adsorbent.

Acknowledgements

Financial supports from the Science and Technology Planning Project of Guangdong Province, China (Grant No. 2017B020237003) and National Natural Science Foundation of China (Grant No. 41472045, 41672042 and 41802041) and Youth Innovation Promotion Association CAS for the excellent members (2016-81-01) and Natural Science Foundation for Distinguished Young Scientists of Guangdong Province (Grant No. 2016A030306034) are gratefully acknowledged. This is a contribution (No. IS-2608) from GIGCAS.

References

Aivalioti, M., Vamvasakis, I., Gidarakos, E., 2010. BTEX and MTBE adsorption onto raw and thermally modified diatomite. J. Hazard. Mater. 178, 136–143.
Amari, A., Chlendi, M., Gannouni, A., Bellagi, A., 2010. Optimised activation of bentonite for toluene adsorption. Appl. Clay Sci. 47, 457–461.
Arai, Y., Sparks, D.L., Davis, J.A., 2005. Arsenate adsorption mechanisms at the allophane-water interface. Environ. Sci. Technol. 39, 2537–2544.
Belaissaoui, B., Le Moullec, Y., Favre, E., 2016. Energy efficiency of a hybrid membrane/condensation process for VOC (volatile organic compounds) recovery from air: a generic approach. Energy 95, 291–302.
Bishop, J.L., Ethbrampe, E.B., Bish, D.L., Abidin, Z.L., Baker, L.L., Matsue, N., Henmi, T., 2013. Spectral and hydration properties of allophane and imogolite. Clay Clay Miner. 61, 57–74.
Brunauer, S., Emmett, P.H., Teller, E., 1938. Adsorption of gases in multimolecular layers. J. Am. Chem. Soc. 60, 309–319.
De Mallmann, A., Barthomeuf, D., 1988. Change in benzene adsorption with acidobasicity of (Cs, Na) X zeolites studied by ir spectroscopy. Zeolites 8, 292–301.
Deng, L., Yuan, P., Liu, D., Annabi-Bergaya, F., Zhou, J., Chen, F., Liu, Z., 2017. Effects of microstructure of clay minerals, montmorillonite, kaolinite and halloysite, on their benzene adsorption behaviors. Appl. Clay Sci. 143, 184–191.
Doble, M., 2006. Biological treatment of VOCs. Chem. Eng. (N. Y.) 113, 35–41.
Dong, G.R., Zhang, Y., 2013. Diatomite modification and its adsorption of heavy metal ions. Adv. Mater. Res. 864-867, 664–667.
Dragoi, B., Dumitriu, E., Guimon, C., Auroux, A., 2009. Acidic and adsorptive properties of SBA-15 modified by aluminum incorporation. Microporous Mesoporous Mater. 121, 7–17.
Du, Y., Wang, H., Chen, S., 2002. Study on alkylation of benzene with ethylene over β-zeolite catalyst to ethylbenzene by in situ IR. J. Mol. Catal. A Chem. 179, 253–261.
Du, P., Yuan, P., Thill, A., Annabi-Bergaya, F., Liu, D., Wang, S., 2017. Insights into the formation mechanism of imogolite from a full-range observation of its sol-gel growth. Appl. Clay Sci. 150, 115–124.
Du, P., Yuan, P., Liu, D., Wang, S., Song, H., Guo, H., 2018. Calcination-induced changes in structure, morphology, and porosity of allophane. Appl. Clay Sci. 158, 211–218.
Farmer, V.C., Fraser, A.R., Tait, J.M., 1979. Characterization of the chemical structures of natural and synthetic aluminosilicate gels and sols by infrared spectroscopy. Geochim. Cosmochim. Acta 43, 1417–1420.
GarcíA, T., Murillo, R., Cazorla-Amorós, D., Mastral, A.M., Linares-Solano, A., 2004. Role of the activated carbon surface chemistry in the adsorption of phenanthrene. Carbon 42, 1683–1689.
Gregg, S., Sing, K., 1982. Adsorption, Surface Area and Porosity. Vol. 3 Acad. Press, London.
Hadjar, H., Hamdi, B., Ania, C.O., 2011. Adsorption of p-cresol on novel diatomite/carbon composites. J. Hazard. Mater. 188, 304–310.
Hallquist, M., Wenger, J., Baltensperger, U., Rudich, Y., Simpson, D., Claeys, M., Dommen, J., Donahue, N., George, C., Goldstein, A., 2009. The formation, properties and impact of secondary organic aerosol: current and emerging issues. Atmos. Chem. Phys. 9, 5155–5236.
Hanudin, E., Matsue, N., Henmi, T., 1999. Adsorption of some low molecular weight organic acids on nano-ball allophane. Clay Sci. 11, 57–72.
Henmi, T., Tange, K., Minagawa, T., Yoshinaga, N., 1981. Effect of SiO_2/Al_2O_3 ratio on

the thermal reactions of allophane. II. Infrared and X-ray powder diffraction data. Clay Clay Miner. 29, 124–128.
Hu, Q., Li, J.J., Hao, Z.P., Li, L.D., Qiao, S.Z., 2009. Dynamic adsorption of volatile organic compounds on organofunctionalized SBA-15 materials. Chem. Eng. J. 149, 281–288.
Iyoda, F., Hayashi, S., Arakawa, S., John, B., Okamoto, M., Hayashi, H., Yuan, G., 2012. Synthesis and adsorption characteristics of hollow spherical allophane nano-particles. Appl. Clay Sci. 56, 77–83.
Jara, A.A., Violante, A., Pigna, M., María, D.L.L.M., 2006. Mutual interactions of sulfate, oxalate, citrate, and phosphate on synthetic and natural allophanes. Soil Sci. Soc. Am. J. 70, 337–346.
Johan, E., Matsue, N., Henmi, T., 1997. Phosphate adsorption on nano-ball allophane and its molecularn orbital analysis. Clay Sci. 10, 259–270.
Kamal, M.S., Razzak, S.A., Hossain, M.M., 2016. Catalytic oxidation of volatile organic compounds (VOCs)–a review. Atmos. Environ. 140, 117–134.
Kawachi, T., Matsuura, Y., Iyoda, F., Arakawa, S., Okamoto, M., 2013. Preparation and characterization of DNA/allophane composite hydrogels. Colloid Surf. B 112, 429–434.
Kroll, J.H., Seinfeld, J.H., 2008. Chemistry of secondary organic aerosol: formation and evolution of low-volatility organics in the atmosphere. Atmos. Environ. 42, 3593–3624.
Lillo-Ródenas, M.A., Cazorla-Amorós, D., Linares-Solano, A., 2005. Behaviour of activated carbons with different pore size distributions and surface oxygen groups for benzene and toluene adsorption at low concentrations. Carbon 43, 1758–1767.
Lin, J.X., Zhan, S.L., Fang, M.H., Qian, X.Q., 2007. The adsorption of dyes from aqueous solution using diatomite. J. Porous. Mater. 14, 449–455.
Liu, D., Yuan, P., Tan, D., Liu, H., Wang, T., Fan, M., Zhu, J., He, H., 2012. Facile preparation of hierarchically porous carbon using diatomite as both template and catalyst and methylene blue adsorption of carbon products. J. Colloid Interface Sci. 388, 176–184.
Matsuura, Y., Iyoda, F., Arakawa, S., John, B., Okamoto, M., Hayashi, H., 2013. DNA adsorption characteristics of hollow spherule allophane nano-particles. Mater. Sci. Eng. C 33, 5079–5083.
Montarges-Pelletier, E., Bogenez, S., Pelletier, M., Razafitianamaharavo, A., Ghanbaja, J., Lartiges, B., Michot, L., 2005. Synthetic allophane-like particles: textural properties. Colloid Surf. A 255, 1–10.
Nishikiori, H., Shindoh, J., Takahashi, N., Takagi, T., Tanaka, N., Fujii, T., 2009. Adsorption of benzene derivatives on allophane. Appl. Clay Sci. 43, 160–163.
Nishikiori, H., Furukawa, M., Fujii, T., 2011. Degradation of trichloroethylene using highly adsorptive allophane–TiO_2 nanocomposite. Appl. Catal. B Environ. 102, 470–474.
Ohashi, F., Wada, S.I., Suzuki, M., Maeda, M., Tomura, S., 2002. Synthetic allophane from high-concentration solutions: nanoengineering of the porous solid. Clay Miner. 37, 451–456.
Okada, K., Nishimuta, K., Kameshima, Y., Nakajima, A., 2005. Effect on uptake of heavy metal ions by phosphate grafting of allophane. J. Colloid Interface Sci. 286, 447–454.
Palazov, A., 1973. Benzene adsorption and its interaction with carbon monoxide on alumina-supported platinum—an infrared spectroscopic study. J. Catal. 30, 13–20.
Pantoja, M.L., Jones, H., Garelick, H., Mohamedbakr, H.G., Burkitbayev, M., 2014. The removal of arsenate from water using iron-modified diatomite (D-Fe): isotherm and column experiments. Environ. Sci. Pollut. Res. Int. 21, 495.
Parfitt, R., 1990. Allophane in New Zealand-a review. Soil Res. 28, 343–360.
Parfitt, R.L., Hemni, T., 1980. Structure of some allophanes from New Zealand. Clay Clay Miner. 28, 285–294.
Pöschl, U., 2005. Atmospheric aerosols: composition, transformation, climate and health effects. Angew. Chem. Int. Ed. 44, 7520–7540.
Rampe, E., Kraft, M., Sharp, T., Golden, D., Ming, D., Christensen, P., 2012. Allophane detection on Mars with thermal emission spectrometer data and implications for regional-scale chemical weathering processes. Geology 40, 995–998.
Serrano, D.P., Calleja, G., Botas, J.A., Gutierrez, F.J., 2007. Characterization of adsorptive and hydrophobic properties of silicalite-1, ZSM-5, TS-1 and Beta zeolites by TPD techniques. Sep. Purif. Technol. 54, 1–9.
Song, W., Justice, R., Jones, C., Grassian, V., Larsen, S., 2004. Synthesis, characterization, and adsorption properties of nanocrystalline ZSM-5. Langmuir 20, 8301–8306.
Thill, A., 2016. Characterisation of imogolite by microscopic and spectroscopic methods. In: Yuan, P., Thill, A., Bergaya, F. (Eds.), Nanosized Tubular Clay Minerals Halloysit and Imogolite. Developments in Clay Science. Vol. 7. Elsevier, Amsterdam, pp. 223–253.
Thommes, M., Kaneko, K., Neimark, A.V., Olivier, J.P., Rodriguez-Reinoso, F., Rouquerol, J., Sing, K.S., 2015. Physisorption of gases, with special reference to the evaluation of surface area and pore size distribution (IUPAC Technical Report). Pure Appl. Chem. 87, 1051–1069.
Yang, F., Ning, Z., Liu, H., 2014. Fractal characteristics of shales from a shale gas reservoir in the Sichuan Basin, China. Fuel 115, 378–384.
Yoon, Y.H., Nelson, J.H., 1984. Application of gas adsorption kinetics I. a theoretical model for respirator cartridge service life. Am. Ind. Hyg. Assoc. J. 45, 509–516.
Yu, W., Deng, L., Yuan, P., Liu, D., Yuan, W., Chen, F., 2015a. Preparation of hierarchically porous diatomite/MFI-type zeolite composites and their performance for benzene adsorption: the effects of desilication. Chem. Eng. J. 270, 450–458.
Yu, W., Yuan, P., Liu, D., Deng, L., Yuan, W., Tao, B., Cheng, H., Chen, F., 2015b. Facile preparation of hierarchically porous diatomite/MFI-type zeolite composites and their performance of benzene adsorption: the effects of NaOH etching pretreatment. J. Hazard. Mater. 285, 173–181.
Yu, W., Deng, L., Yuan, P., Liu, D., Yuan, W., Liu, P., He, H., Li, Z., Chen, F., 2015c. Surface silylation of natural mesoporous/macroporous diatomite for adsorption of benzene. J. Colloid Interface Sci. 448, 545–552.
Yuan, P., Yang, D., Lin, Z., He, H., Wen, X., Wang, L., Deng, F., 2006. Influences of pretreatment temperature on the surface silylation of diatomaceous amorphous silica with trimethylchlorosilane. J. Non-Cryst. Solids 352, 3762–3771.
Yuan, P., Liu, D., Fan, M., Yang, D., Zhu, R., Ge, F., Zhu, J., He, H., 2010. Removal of hexavalent chromium [Cr(VI)] from aqueous solutions by the diatomite-supported/unsupported magnetite nanoparticles. J. Hazard. Mater. 173, 614–621.
Yuan, P., Tan, D., Aannabi-Bergaya, F., Yan, W., Fan, M., Liu, D., He, H., 2012. Changes in structure, morphology, porosity, and surface activity of mesoporous halloysite nanotubes under heating. Clay Clay Miner. 60, 561–573.
Yuan, P., Liu, D., Tan, D., Liu, K., Yu, H., Zhong, Y., Yuan, A., Yu, W., He, H., 2013. Surface silylation of mesoporous/macroporous diatomite (diatomaceous earth) and its function in Cu(II) adsorption: the effects of heating pretreatment. Microporous Mesoporous Mater. 170, 9–19.
Yuan, P., Tan, D., Annabi-Bergaya, F., 2015a. Properties and applications of halloysite nanotubes: recent research advances and future prospects. Appl. Clay Sci. 112, 75–93.
Yuan, W., Yuan, P., Liu, D., Yu, W., Deng, L., Chen, F., 2015b. Novel hierarchically porous nanocomposites of diatomite-based ceramic monoliths coated with silicalite-1 nanoparticles for benzene adsorption. Microporous Mesoporous Mater. 206, 184–193.
Yuan, W., Yuan, P., Liu, D., Deng, L., Zhou, J., Yu, W., Chen, F., 2016. A hierarchically porous diatomite/silicalite-1 composite for benzene adsorption/desorption fabricated via a facile pre-modification in situ synthesis route. Chem. Eng. J. 294, 333–342.
Zhao, X., Ma, Q., Lu, G., 1998. VOC removal: comparison of MCM-41 with hydrophobic zeolites and activated carbon. Energy Fuel 12, 1051–1054.